



# Plasmonic Bi nanoparticles and BiOCl sheets as cocatalyst deposited on perovskite-type $ZnSn(OH)_6$ microparticle with facet-oriented polyhedron for improved visible-light-driven photocatalysis



Hou Wang <sup>a,b,c</sup>, Xingzhong Yuan <sup>a,b,\*</sup>, Yan Wu <sup>c,\*\*\*</sup>, Guangming Zeng <sup>a,b</sup>, Wenguang Tu <sup>d</sup>, Chong Sheng <sup>d</sup>, Yaocheng Deng <sup>a,b</sup>, Fei Chen <sup>a,b</sup>, Jia Wei Chew <sup>c,e,\*\*\*</sup>

<sup>a</sup> College of Environmental Science and Engineering, Hunan University, Changsha 410082, PR China

<sup>b</sup> Key Laboratory of Environment Biology and Pollution Control, Hunan University, Ministry of Education, Changsha 410082, PR China

<sup>c</sup> School of Chemical and Biomedical Engineering, Nanyang Technological University, Singapore 637459, Singapore

<sup>d</sup> National Laboratory of Solid State Microstructures & Department of Physics, Nanjing University, Nanjing 210093, China

<sup>e</sup> Singapore Membrane Technology Center, Nanyang Environment and Water Research Institute, Nanyang Technological University, Singapore 639798, Singapore

## ARTICLE INFO

### Article history:

Received 20 November 2016

Received in revised form 16 February 2017

Accepted 4 March 2017

Available online 6 March 2017

### Keywords:

Perovskite-type  $ZnSn(OH)_6$   
Plasmonic Bi nanoparticles  
Photocatalysis  
Exposure facets

## ABSTRACT

Perovskite-type structure materials have attracted considerable attention in the field of solar cell and photocatalysis. In this study, novel plasmonic Bi nanoparticles and BiOCl sheets co-decorated  $ZnSn(OH)_6$  (ZSH) with various morphologies (hence exposure facets) was successfully synthesized via one-pot precipitation, hydrolysis and UV-photoreduction process. The as-obtained materials were characterized by field emission scanning electron microscopy, transmission electron microscopy, X-ray diffraction, X-ray photoelectron spectroscopy, ultraviolet-visible diffuse reflection spectroscopy and photocurrent-time measurement. Results indicated that the cubic, 14-facets polyhedral and octahedral ZSH were decorated by plasmonic Bi particles and BiOCl sheets, which improved visible-light absorption, charge carrier separation and migration performance. Compared with pure ZSH, the composites showed enhanced photocatalytic activity, with the highest photocatalytic performance achieved by the octahedral ZSH decorated by Bi and BiOCl (i.e., ZSH-3-Bi). The photo-degradation rate of ZSH-3-Bi was about 81 times higher than that of pure octahedral ZSH. This phenomenon was mainly ascribed to the surface plasmon resonance effect for visible light absorption, the exposed {111} facets relative to other facets of octahedral ZSH, and the improved charge carrier separation efficiency due to the strong interfacial interaction of three components. The radical and hole trapping, and electron spin resonance spin-trap experiments verified that the  $\cdot OH$ ,  $\cdot O_2^-$  and  $h^+$  were the main reactive species in this system, which were responsible for the decoloration and part mineralization of the RhB molecules. Therefore, this work provides new insights into the in situ fabrication of plasmonic Bi-based photocatalyst with facet-oriented polyhedron for full utilization of solar energy and wastewater treatment.

© 2017 Elsevier B.V. All rights reserved.

## 1. Introduction

In the field of solar-to-chemical energy conversion, semiconductor-based photocatalysis have attracted considerable

research attention for photochemical synthesis, environmental cleaning and energy production [1–4]. Recently, perovskite materials are not only promising in solar to electricity generation like perovskite solar cells, but also have attracted attention in photocatalytic reaction in environmental pollutant removal in aqueous solution as well as water splitting for hydrogen production [5–9]. The ideal perovskite-type  $ABX_3$  structure has a cubic symmetry with space group  $Pm\bar{3}m$ , whereby the B is a 6-fold coordinated cation and the A is a 12-fold cubooctahedral coordinated cation, surrounded by an octahedron of the X anions. Zinc hydroxystannate ( $ZnSn(OH)_6$ ; ZSH), a member of composite metal hydroxide, is a kind of perovskite structure (Fig. 1) tending

\* Corresponding author at: College of Environmental Science and Engineering, Hunan University, Changsha 410082, PR China.

\*\* Corresponding author.

\*\*\* Corresponding author at: School of Chemical and Biomedical Engineering, Nanyang Technological University, Singapore 637459, Singapore.

E-mail addresses: [yxz@hnu.edu.cn](mailto:yxz@hnu.edu.cn) (X. Yuan), [wuyan1101@126.com](mailto:wuyan1101@126.com) (Y. Wu), [JChew@ntu.edu.sg](mailto:JChew@ntu.edu.sg) (J.W. Chew).

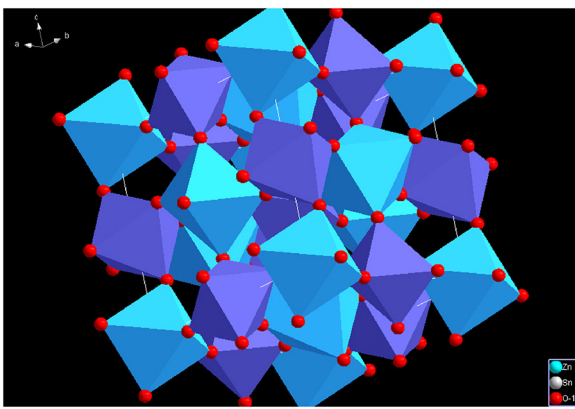


Fig. 1. Schematic structure of  $\text{ZnSn}(\text{OH})_6$  (ZSH).

to form face-centered-cubic crystal structure and is filled with hydroxyl groups on the surface [10]. Much attention has been paid to potential applications of ZSH in gas sensing, lithium-ion batteries and photocatalysis [11–13]. Compared with commercial  $\text{TiO}_2$ , the ZHS has showed much higher conversion and mineralization of persistent organic pollutant such as benzene, methylene blue and methyl orange under UV irradiation [12,14–16]. The high and stable activity of ZHS was mainly attributed to the abundance of surface  $\text{OH}^-$  groups which accept photogenerated holes to yield highly reactive radical  $\cdot\text{OH}$  radicals, and the facile regeneration of  $\cdot\text{OH}$  groups whose process involves the participation of  $\text{O}_2^{\bullet-}$  and  $\text{H}_2\text{O}$ .

Unfortunately,  $\text{ZnSn}(\text{OH})_6$  (ZSH), which has a wide band-gap energy of 4.0 eV, can only use the UV fraction, which represents only ~4% of solar light [10]. During the UV-photocatalytic process, the surface hydroxyls of ZSH can accept photo-generated holes to form hydroxyl radicals, thereby triggering the photocatalytic oxidation reactions. Fu et al. prepared four different kinds of ZSH microparticles through grinding, co-precipitation, self-templating, and hydrothermal processes [12], among which the highest photocatalytic activity and stability for the degradation of methyl orange and gaseous  $\text{C}_6\text{H}_6$  under UV irradiation was obtained by the ZSH synthesized via the polyvinyl pyrrolidone-assisted hydrothermal method. Yu et al. studied the controllable synthesis of crystallographic facet-oriented polyhedral ZSH microcrystals with the assistance of the  $\text{OH}^-$  ion [17], which resulted in the {111} facet being more UV-light driven photocatalytically active than {100} for the conversion and mineralization of benzene.

Combining ZSH with narrow band gap semiconductor or metal nanoparticles is a promising approach to expand the optical response of semiconductor from UV to visible light region and improve the photocatalytic activity. Our group had recently demonstrated that the photocatalytic activity of ZSH could be

promoted by constructing a heterojunction with  $\text{AgI}$  or plasmonic  $\text{Ag}@\text{Ag}_3\text{PO}_4$  nanoparticles [18,19]. The  $\text{Ag}@\text{AgCl}$ (8 wt%)/ZSH heterostructured photocatalyst exhibited outstanding photocatalytic performance, with the degradation rates for rhodamine B, crystal violet, and phenol solution as high as respectively 22, 15 and 16 times those of pure ZSH and respectively 3.6, 4 and 3.6 times those of the conventional visible-light photocatalyst  $\text{N-TiO}_2$ . Li et al. reported that the light absorption intensity of  $\text{BiOI}/\text{ZSH}$  increased in the 280–550 nm region when the ZSH was covered by  $\text{BiOI}$  nanoparticles [20], which was presumably due to the heterojunction-enhanced photocatalytic activity toward the degradation of phenol and photocatalytic  $\text{H}_2$  production due to the flow of electrons from one phase to another. Wu et al. demonstrated that ZSH hollow nanocubes with plasmonic Au nanoparticles could give a strong light absorption peak in the wavelength range 450–750 nm because of the surface plasmon resonance effect, and the photodegradation activity under visible-light illumination was in the following order:  $\text{Au/ZnSn}(\text{OH})_6 > \text{Au/ZnSnO}_3 > \text{ZnSn}(\text{OH})_6 > \text{ZnSnO}_3$  [21].

Deposition of noble metal nanoparticles (like Au [21,22] and Ag [18,23]) on semiconductors is an alternative method to enhance the light absorption range and intensity of ZSH via the formation of Schottky barrier at the interface. Considering the high cost of the precious metals, semimetal bismuth (Bi), which is abundantly available, has attracted intense research interest in the field of photocatalysis [23]. The semimetal bismuth (Bi) has small band overlap energy, low electron effective mass, and low charge carrier density. Previous investigations had shown that Bi nanoparticles (including nanobundles, nanowire) exhibited surface plasmon resonance effect and could serve as the electron trap, which was sensitive to the size, shape and organization of nanoparticles [24–27]. Gao et al. prepared hierarchical Bi based nanobundles via the self-assembled technology with the aid of hydrazine hydrate as a reducing agent [26], resulting in a photocatalyst with a degradation efficiency of 96% for Rhodamine B dye after 90 min of exposure to visible light. Dai's group synthesized  $\text{BiVO}_4$ -based materials via the alcoho-hydrothermal strategy, polymethyl methacrylate-templating and polyvinyl pyrrolidone-assisted reduction methods and the as-obtained photocatalyst showed excellent photocatalytic performance for the removal of phenol, rhodamine B, methylene blue and 4-chlorophenol [28–30]. Meanwhile, several semiconductors, coupled with Bi nanoparticles to achieve an ideal efficiency, had also been investigated, including  $\text{g-C}_3\text{N}_4$  [31],  $\text{BiOCl}$  [32],  $\text{ZnWO}_4$  [33],  $(\text{BiO})_2\text{CO}_3$  [34–37],  $\text{Bi}_2\text{O}_3/\text{Bi}_2\text{S}_3$  [38,39],  $\text{Bi}_2\text{MoO}_6$  [40],  $\text{Bi}_2\text{WO}_6$  [41], and  $\text{TiO}_2$  [42]. For example, Dong et al. found that the addition of Bi nanoparticles resulted in higher visible light photocatalytic activity and oxidation ability for  $\text{NO}$  oxidation, due to the surface plasmon resonance effect on the surface of  $(\text{BiO})_2\text{CO}_3$  microspheres conferring more efficient separation of electron–hole pairs and prolonging lifetime of charge carriers [35]. However, no study has been conducted to date on the effect of the combina-

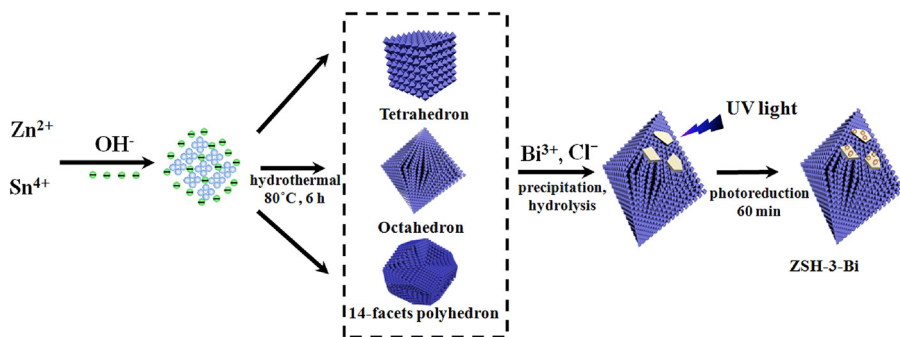
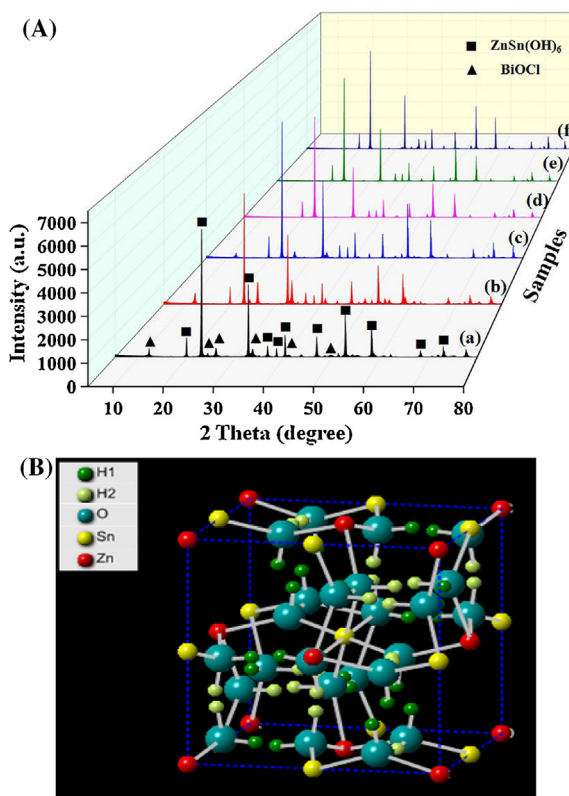


Fig. 2. Schematic presentation of the synthesis of the ZSH-Bi micro-structure.



**Fig. 3.** (A) XRD patterns of (a) ZSH-1-Bi, (b) ZSH-2-Bi, (c) ZSH-3-Bi, (d) ZSH-1, (e) ZSH-2 and (f) ZSH-3; (B) 3D-unit cell crystal structure of ZSH-3.

tion of Bi nanoparticles and  $\text{BiOCl}$  sheets deposited onto different exposure facet of the ZSH polyhedron to promote the charge separation and visible light-driven photocatalytic performance. The  $\{111\}$ ,  $\{100\}$ , and  $\{110\}$  facets of ZSH are different in terms of surface atom density, electronic structure, bonding energy and possibly chemical reactivity [17,43,44]. Correspondingly, the photocatalytic activity of different exposure facets of ZSH after the introduction of plasmonic Bi nanoparticles and  $\text{BiOCl}$  sheet may be different under visible light exposure. In this study, the cubic, 14-facets polyhedral and octahedral ZSH were firstly synthesized by the hydrothermal method, followed by the introduction of Bi nanoparticles and  $\text{BiOCl}$  sheets on the surface of ZSH via precipitation, hydrolysis and UV-photo reduction. The resultant composite were characterized comprehensively by means of XRD, FESEM, TEM, XPS, UV-vis DRS, PL spectroscopy and photocurrent-time test. This environmentally friendly composite was found to show superior photocatalytic activity toward Rhodamine B dye degradation under visible light irradiation. The mechanism underlying the enhanced photocatalytic activity was also investigated.

## 2. Experimental

### 2.1. Materials

Zinc acetate ( $\text{ZnAc}_2$ ), tin chloride ( $\text{SnCl}_4$ ), sodium hydroxide ( $\text{NaOH}$ ), ethanol ( $\text{C}_2\text{H}_5\text{O}$ ), bismuth chloride ( $\text{BiCl}_3$ ), carbon disulfide ( $\text{CS}_2$ ) and sulfur powder were purchased from Sinopharm Chemical Reagent Co., Ltd. (Shanghai, China). All reagents and solvents were of analytical reagent grade and used as received from commercial suppliers.

### 2.2. Synthesis of $\text{ZnSn(OH)}_6$

In a typical synthesis, an aqueous solution of  $\text{SnCl}_4$  (0.5 M, 25 mL) was added to a solution of  $\text{ZnAc}_2$  (0.5 M, 25 mL) in a beaker and agitated vigorously at room temperature before a solution of sodium hydroxide ( $\text{NaOH}$ , 50 mL) with the desired concentration was added to the mixture at the molar ratios of  $\text{SnCl}_4:\text{ZnAc}_2:\text{NaOH}=1:1:X$  (whereby  $X=6.5, 10.5$  or 15). The mixed solution was heated to  $80^\circ\text{C}$  and stirred (600 rpm/min) for 6 h under reflux condensation. After the reaction, the precipitate was collected by centrifugation, and washed with deionized water and ethanol three times. The final products were then dried in air at  $70^\circ\text{C}$  for 12 h before characterization. The obtained materials with the morphological modification of cubic, 14-facets polyhedral and octahedral ZSH are denoted here respectively as ZSH-1, ZSH-2 and ZSH-3.

### 2.3. Synthesis of $\text{Bi/BiOCl/ZnSn(OH)}_6$ (ZSH-Bi)

A mixture of 5 mL  $\text{CS}_2$  and 48 mg sulfur powder was added to 100 mL ethanol with vigorous stirring for 5 min until the solids were completely dissolved. The ZSH powder with different morphologies (i.e., cubic, 14-facets polyhedral and octahedral) was dispersed into the clear solution via sonication for 20 min. Then 1 mmol  $\text{BiCl}_3$  was dissolved into the above mixture with the aid of sonication. Nitrogen gas was bubbled into the suspension for 60 min in the dark. After that, the suspension was irradiated with ultraviolet light for 1 h. The product was centrifuged, and washed with ethanol and deionized water for three times, and then vacuum dried at  $70^\circ\text{C}$  for 12 h. The details are illustrated in Fig. 2. The obtained materials from the cubic, 14-facets polyhedral and octahedral ZSH can be denoted respectively as ZSH-1-Bi, ZSH-2-Bi and ZSH-3-Bi.

### 2.4. Analytical methods

Bruker AXS D8 Advance diffractometer operating with  $\text{Cu K}\alpha$  source was used to record the powder X-ray diffraction (XRD) patterns. The morphology of the photocatalyst was observed via field emission scanning electron microscopy (FESEM) (JSM-7001F, Japan) and transmission electron microscopy (TEM) (Tecnai G2 F20 S-Twin, USA) [45]. The chemical component and electronic state was investigated by X-ray photoelectron spectroscopy (Thermo Fisher Scientific, UK). UV-visible diffuse-reflectance spectra (UV-vis DRS) were recorded in the range of 200–800 nm with a Varian Cary 300 spectrometer. Three-dimensional excitation-emission matrix fluorescence spectra (3D EEMs) were collected in the excitation wavelength range of  $\lambda_{\text{ex}}=350\text{--}650\text{ nm}$  and in the emission wavelength range of  $\lambda_{\text{em}}=400\text{--}800\text{ nm}$  (F-4500 spectrofluorimeter, Hitachi, Japan); the detailed method had been previously reported [46]. Photoluminescence (PL) spectroscopy was measured at the excitation wavelength of 280 nm at room temperature. The total organic carbon (TOC) assays were carried out using a Shimadzu TOC-VCPh analyzer. Photocurrent-time (PT) was tested with a CHI 660C electrochemical station in a standard three electrode configuration [47]. The electron spin resonance (ESR) signals of radicals spin-trapped by spin-trapped reagent 5, 5-dimethyl-1-pyrroline N-oxide (DMPO) and 2,2,6,6-Tetramethylpiperidinooxy (TEMPO) were examined via a Bruker ER200-SRC spectrometer under visible light irradiation ( $\lambda>420\text{ nm}$ ).

### 2.5. Photocatalytic experiment

Photocatalytic activity of the samples was tested by the photocatalytic decomposition of RhB with visible light illumination ( $\lambda>420\text{ nm}$ ) after the adsorption process. A 300 W Xenon lamp

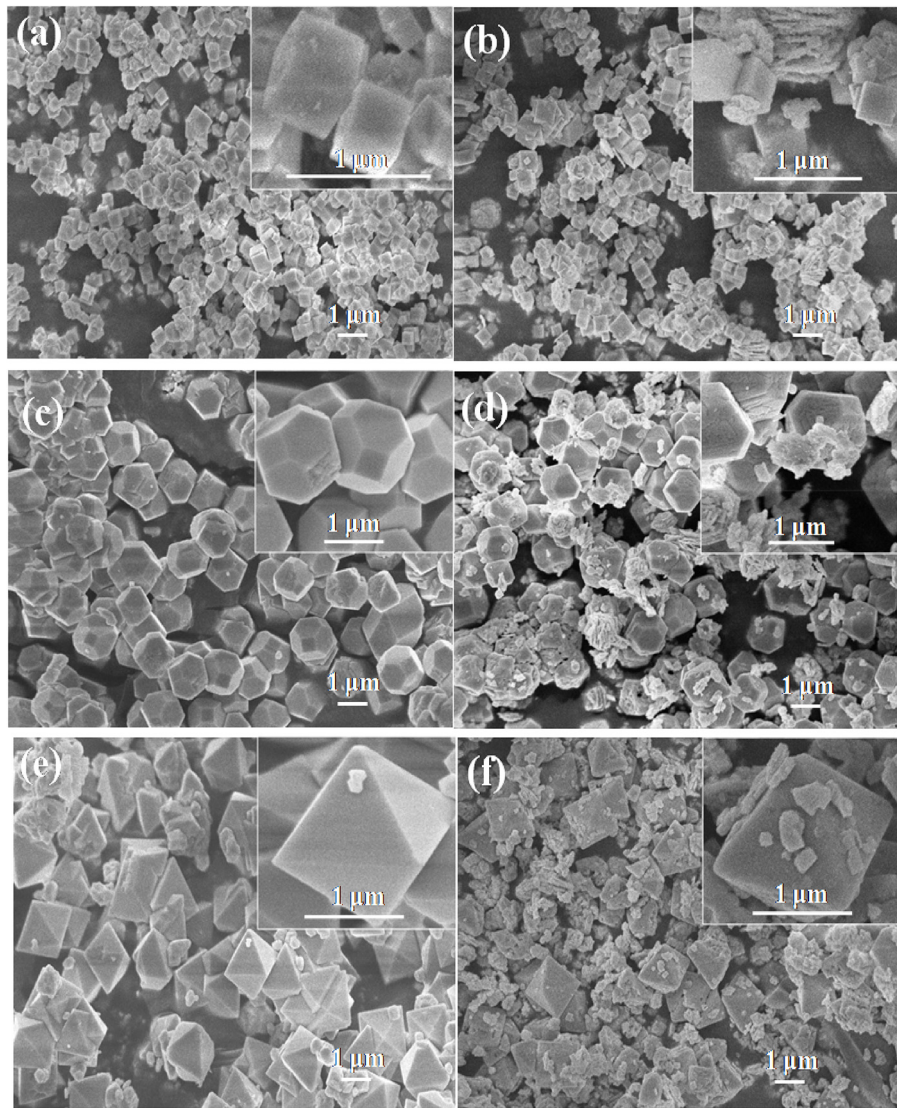


**Fig. 4.** SEM images of (a) ZSH-1, (b) ZSH-1-Bi, (c) ZSH-2, (d) ZSH-2-Bi, (e) ZSH-3 and (f) ZSH-3-Bi.

(CEL-HXF300, Beijing CEL Tech. Co., Ltd.) with a 420 nm cutoff filter was used as the visible light source (14V, 16A, at a distance 15 cm from the photocatalytic reactor). The light intensity of the 300 W Xenon lamp was 300 mW cm<sup>-2</sup>. For the decomposition of RhB, 100 mg of photocatalyst was dispersed in 100 mL of 48 mg L<sup>-1</sup> RhB aqueous solution. Prior to irradiation, the suspension was magnetically stirred in the dark for 60 min to get the adsorption–desorption equilibrium between photocatalyst and RhB. At certain time intervals, samples were collected via centrifugation to remove the particles (10,000 rpm/min). The RhB concentration before and after photo-degradation were monitored with a UV-vis spectrophotometer (UV-2250, SHIMADZU Corporation, Japan) at the wavelength of 554 nm.

### 3. Results and discussion

#### 3.1. Characterization

The crystallographic structure of as-prepared ZSH and ZSH-Bi samples were confirmed by the XRD spectra (Fig. 3A). For pure ZSH (Fig. 3Ad–f), the sharp and intense diffraction peaks can be indexed to the standard cubic phase of high-purity ZSH crystals (JCPDS file no. 73-2384). The detailed ball-stick model of the octahedral ZSH

crystal structure (ZSH-3) is shown in Fig. 3B. The intense diffraction peaks at  $2\theta = 19.7^\circ, 22.8^\circ, 32.4^\circ, 36.4^\circ, 38.2^\circ, 40.0^\circ, 46.5^\circ, 52.4^\circ, 57.8^\circ, 67.9^\circ$  and  $72.6^\circ$  are associated with the (111), (200), (220), (013), (311), (222), (400), (422), (440) and (442) planes in ZSH, respectively. After the photodeposition reaction, the new diffraction peaks appear at  $2\theta = 12.0^\circ, 24.2^\circ, 25.9^\circ, 33.5^\circ, 41.0^\circ$  and  $49.5^\circ$ , which corresponds respectively to the (001), (002), (101), (102), (112) and (004) planes of the tetragonal BiOCl phase (JCPDS file no. 82-0485) [48,49]. XRD analysis of the composites indicated that the introduction of BiOCl did not destroy the phase structure of ZSH.

The surface morphology of as-obtained samples measured by SEM is presented in Fig. 4(a–f). It is clear that ZSH-1 (Fig. 4a), ZSH-2 (Fig. 4b) and ZSH-3 (Fig. 4c) have shapes corresponding respectively to cubes, 14-facets polyhedrons and octahedrons, with smooth surfaces and uniform sizes. It could be due to that the OH<sup>-</sup> ions concentration in solution adjust adsorption kinetics of crystal surface, controlled the facet area ratios, and thus led to different morphology and size of pure ZSH [17]. The sizes of these microcrystals are in the range of 0.7–2.0 μm. After the photodeposition reaction under ultraviolet light exposure in the presence of BiCl<sub>3</sub>, a large amount of BiOCl sheets appeared on the surface of ZSH, as seen in Fig. 4b, d and f. This is because Bi<sup>3+</sup> reacted with the OH group of ZSH to form hydroxylated compounds like Bi(OH)<sub>2</sub>Cl when the Bi<sup>3+</sup> and Cl<sup>-</sup>

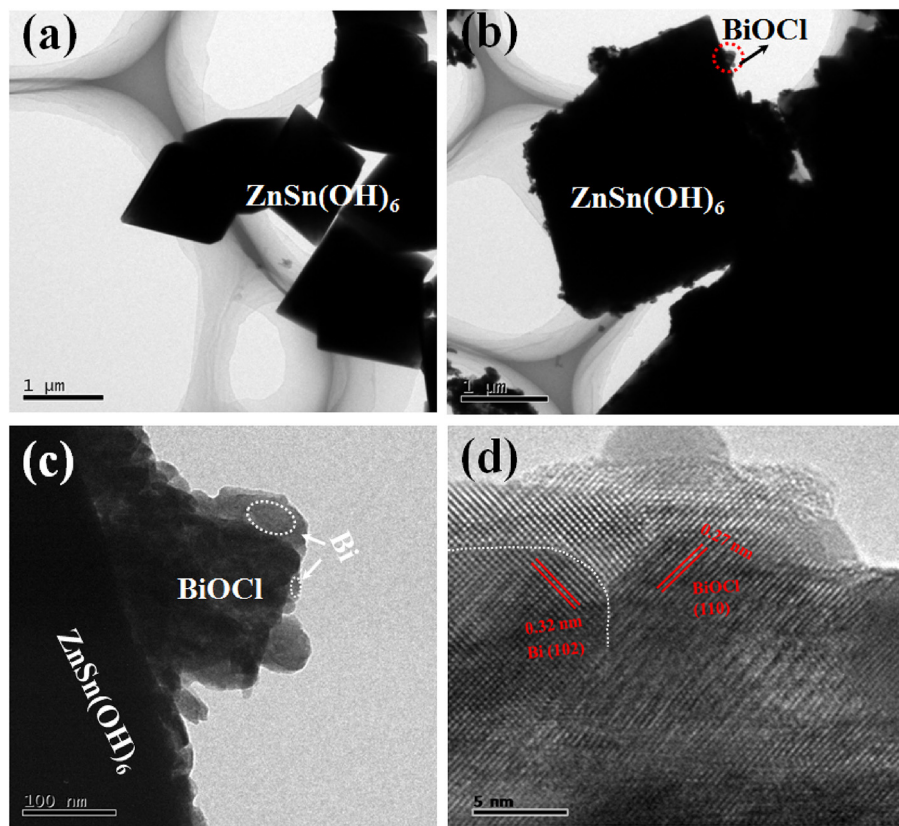


**Fig. 5.** TEM images of pure ZSH-3 (a) and ZSH-3-Bi (b and c). For comparison, the high-resolution TEM image of ZSH-3-Bi (d) is also shown.

were adsorbed onto ZSH, and then dehydration took place between neighboring hydroxyl groups, followed by successive growth with the double chlorine layers to build the O-Bi-Cl sheets stack [32,50].

Although the metallic Bi could not be directly observed in the SEM images due to the small size, the change in sample color (see the inset in Fig. 7) from white to brownish black confirms the presence of Bi nanoparticles in ZSH-3-Bi. In order to represent the microstructure, the typical TEM images of pure ZSH-3 microcrystal and ZSH-3-Bi are shown in Fig. 5. The pure ZSH-3 microcrystal is rhombic with smooth surfaces and a diameter of  $\sim 2 \mu\text{m}$ . For ZSH-3-Bi, Fig. 5b–c shows that the surfaces are rough due to the BiOCl agglomerate sheets attached. Furthermore, many black dots each sized at about 10 nm appear on the surface of BiOCl. HRTEM was further used to observe the roughness elements. Fig. 5d displays two kinds of lattice fringes with  $d$  spacings of about 0.27 nm and 0.32 nm, which can be designated as the (110) and (102) planes of BiOCl and metallic Bi, respectively. The mechanisms leading to such structures are presumably as follows. Because the redox potential of the metal precursors (0.31 eV vs. SHE) is more positive than the conduction band potential of BiOCl ( $-1.1$  eV vs. SHE), on absorbing a photon, a BiOCl particle generates an electron and a hole, and subsequently the photo-generated electron combines with a  $\text{Bi}^{3+}$  ion or  $\text{Bi}^{3+}$  to form a Bi atom. Continuous reduction of Bi ions can produce nucleates or nanoparticles on the surface of BiOCl or ZSH forming a Schottky junction between them. Meanwhile, the corresponding holes are depleted by the ethanol. A similar phenomenon was also observed in our previous research on the synthesis of Ag nanoparticles and metal sulfide quantum dot [23,51].

Furthermore, the chemical composition and valence state of various elements in the pure ZSH-3 and ZSH-3-Bi samples have been characterized by XPS spectra. The survey spectrum in Fig. 6a indicates that the elements Zn, Sn, O, Cl and Bi are present in the ZSH-3-Bi sample while only the peaks of Zn, O and Sn appear in pure

ZSH. The molar ratio of Bi and Cl was about 1.21, which was higher than the theoretical stoichiometric atomic ratio between Bi and Cl species in the pure BiOCl. This confirms the existence of excess Bi on the surface of the ZSH-3-Bi composite. High-resolution XPS spectra (Fig. 6b) in the region of Bi 4f could be resolved into six peaks. The peaks at 158.0 eV and 163.2 eV corresponds to Bi 4f<sub>7/2</sub> and Bi 4f<sub>5/2</sub>, respectively, which are features of the  $\text{Bi}^{3+}$  in BiOCl [34,52]. The other two peaks at 162.0 eV and 156.9 eV correspond to metallic Bi [31,53]. In Fig. 6c, for ZSH-3, only one peak (namely, 530.3 eV) of the O 1s spectra was present, which is associated with the oxygen components (e.g. Zn-O, Sn-O) [18,54]. On the other hand, for ZSH-3-Bi, the O 1s peak was shifted slightly rightwards to 530.5 eV, and two additional peaks at 529.0 eV and 531.6 eV emerged, which correspond respectively to the Bi-O bond and the adsorbed OH on the surface [54,55]. Coupling the rightward shift of the O 1s peak and the new peak at 531.6 eV for ZSH-Bi (Fig. 6c), it can be inferred that heterostructures formed between ZSH-3 and BiOCl.

As displayed in Fig. 6d, there are two peaks at the binding energy values of 1022.2 eV and 1045.3 eV, which correspond to the binding energy of Zn 2p<sub>3/2</sub> and Zn 2p<sub>1/2</sub>, respectively, in ZSH-3. Fig. 6e further shows that, the high-resolution of Sn 3d<sub>5/2</sub> and Sn 3d<sub>3/2</sub> corresponds to the binding energies of 486.9 eV and 495.3 eV, respectively. Interestingly, a small shift of Zn 2p and Sn 3d toward lower binding energy is observed for ZSH-3-Bi as compared to pure ZSH-3, indicating the strong interfacial interaction between the Bi/BiOCl sheets and ZSH-3 microcrystal. Similar results has also been observed by Li et al. [20]. Collectively, the XRD, SEM, TEM and XPS results indicate that Bi/BiOCl/ZnSn(OH)<sub>6</sub> has been successfully synthesized via precipitation, hydrolysis and UV-photoreduction.

The UV-vis absorption spectra was used to determinate the optical property of as-obtained samples. As shown in Fig. 7, pure ZSH-1, ZSH-2 and ZSH-3 samples can only absorb the UV light up to wavelengths of about 330 nm, 384 nm and 394 nm, respectively.

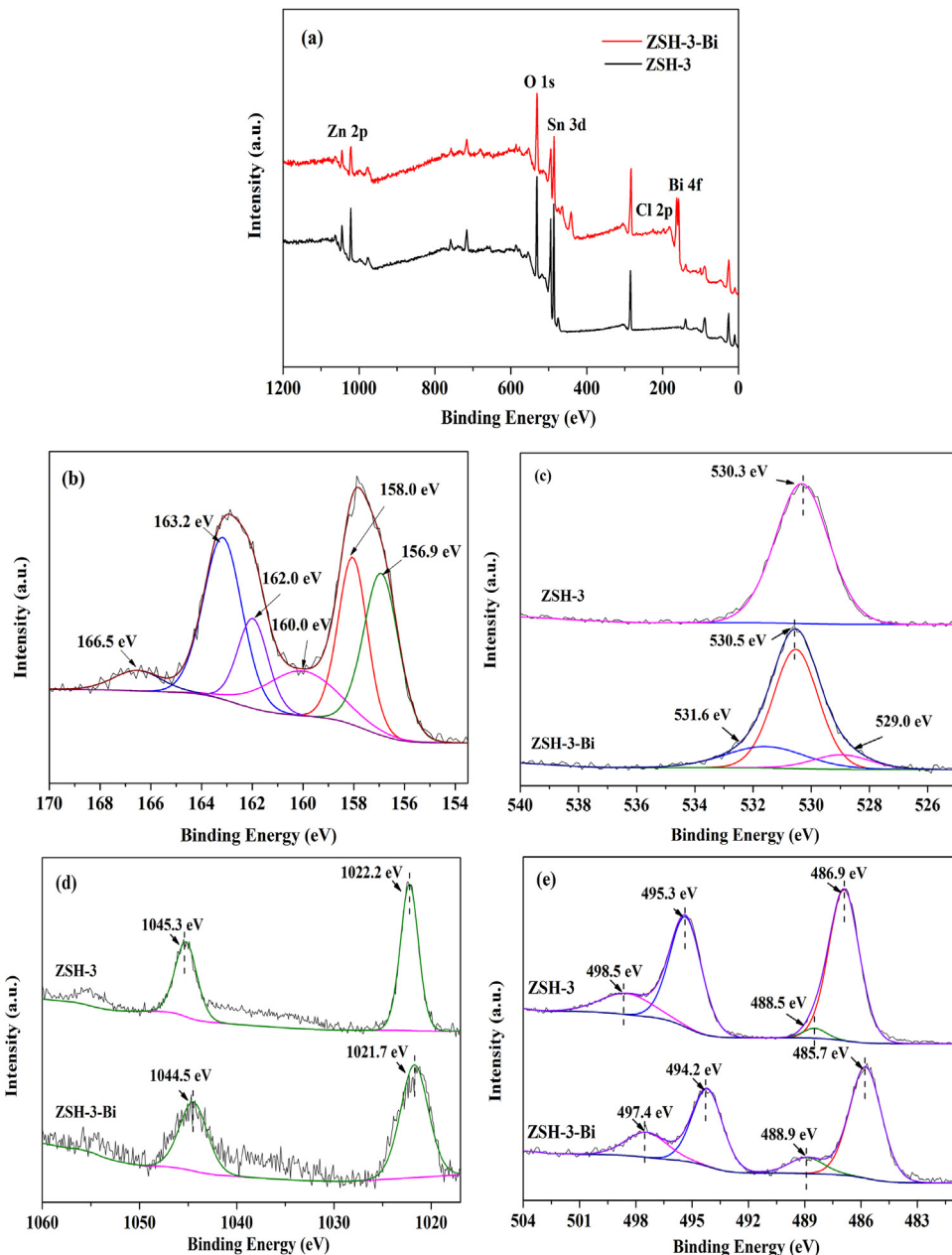


Fig. 6. XPS spectra of ZSH and ZSH-3-Bi: (a) survey scan, (b) Bi 4f, (c) O 1s, (d) Zn 2p and (e) Sn 3d.

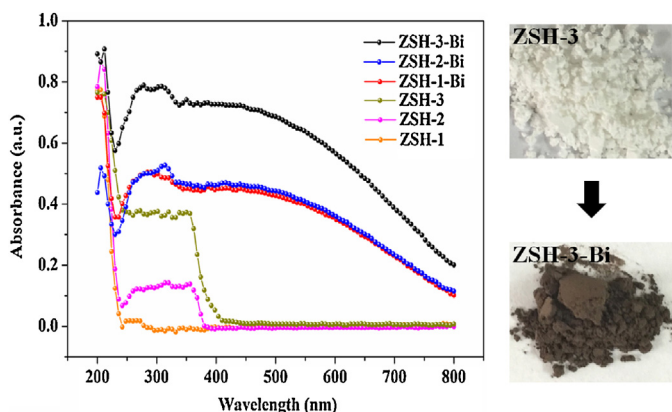
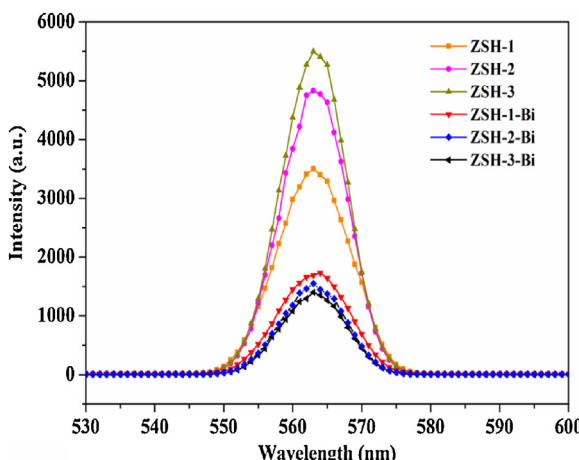


Fig. 7. UV-vis DRS of the as-obtained samples. The inset is the corresponding photograph of ZSH-3 before and after UV irradiation.

Since the band gap ( $E_g$ ) of the photocatalyst can be expressed as  $E_g = 1240/\lambda$  [18], where  $\lambda$  is the uppermost wavelength absorbable, that of ZSH-1, ZSH-2 and ZSH-3 corresponds to 3.76 eV, 3.23 eV and 3.14 eV, respectively. A greater absorption in the UV region along with a narrow band gap is favored for the production of more electron–hole pairs. After the hole was gradually consumed by ethanol, the accumulated electrons would be available for the successive reduction of metallic Bi. Previous reports demonstrated that the non-noble metal Bi exhibited surface plasmon resonance (SPR) property in the near-ultraviolet and visible light range [11,12]. Therefore, for ZSH-1-Bi, ZSH-2-Bi and ZSH-3-Bi, a notable absorption extension into the visible-light region in the range 400–800 nm is observed, which is in accordance with the color change of the samples (the inset of Fig. 7). The main absorption in visible-light region especial in the range 450–750 nm can be ascribed to the SPR absorption of metallic Bi since the optical absorption of pristine BiOCl is usually in the UV region [35,55,56]. Therefore, the strong



**Fig. 8.** Photoluminescence spectra of pure ZSH and the corresponding composites at an excitation wavelength of 280 nm.

interfacial interactions via the combination of metallic Bi, BiOCl and ZSH provide an efficient utilization of visible light, thus producing more electron–hole pairs.

Photo-generated electrons and holes are easily separated in the transfer process, thereby improving quantum efficiency greatly. In order to elucidate the fact that Bi, ZSH and BiOCl can cooperatively improve the separation of light-triggered charge carriers, a photoluminescence (PL) spectroscopy study was performed. Fig. 8 presents the PL spectra of ZSH and ZSH-Bi at an excitation wavelength of 280 nm. All the pure ZSH exhibit higher peak magnitudes at a wavelength of around 563 nm in the PL spectra, which can be attributed to the band gap recombination of electron–hole pairs. Relatively, the peak intensities of ZSH-1-Bi, ZSH-2-Bi and ZSH-3-Bi are weaker, suggesting that the recombination rate of photo-generated electrons and holes slow down [57]. Among them, ZSH-3-Bi have the lowest peak magnitude, which indicates the lowest photo-generated electron–hole ( $e^- - h^+$ ) recombination rate, thereby implying that it exhibits the highest photocatalytic activity.

### 3.2. Photocatalytic activity

The morphology-dependent photocatalytic activity was investigated by RhB degradation in aqueous solution under visible light irradiation (Fig. 9). Before the illumination with visible light, the photocatalysts were firstly mixed with RhB solutions in the dark for an hour to establish the adsorption–desorption equilibrium. Fig. 9a shows that, under visible light irradiation, the degradation of RhB is negligible in the absence of photocatalyst. Similarly, pure ZSH of different morphologies and sizes have insignificant visible-light-driven photocatalytic activity, which is because the pure ZSH can be only activated in the UV region. On the other hand, in the presence of ZSH-Bi photocatalysts, the irradiation of visible light resulted in the obvious degradation of RhB, with the different ZSH morphologies exerting influence on the rate of photocatalytic activity. After 120 min of exposure to visible light, the octahedral ZSH-3-Bi gave the greatest degradation of 91.4%, followed by the cubic ZSH-1-Bi with a degradation of 83.5%, then the 14-facets polyhedral ZSH-2-Bi with a degradation of 65.6%. Assuming a pseudo-first order kinetics model (i.e.,  $\ln(C/C_0) = kt$ ), the values of the rate constant ( $k$ ) are shown in Fig. 9b. The rate constant ( $k$ ) for the RhB degradation was greatest for ZSH-3-Bi ( $0.01952 \text{ min}^{-1}$ ), followed by ZSH-2-Bi ( $0.01469 \text{ min}^{-1}$ ), ZSH-1-Bi ( $0.00871 \text{ min}^{-1}$ ), ZSH-3 ( $0.00024 \text{ min}^{-1}$ ), ZSH-2 ( $0.00020 \text{ min}^{-1}$ ), then finally the lowest for ZSH-1 ( $0.00009 \text{ min}^{-1}$ ). Notably, the photo-degradation rate of ZSH-3-Bi was about 81 times higher than that of pure ZSH-

3, which indicated that the combination of ZSH with Bi and BiOCl was an effective way to improve the photocatalytic activity. The addition of Bi and BiOCl not only extended the range of absorption wavelength from UV to visible light region, but also improved the charge carrier separation by the formation of strong interfacial interaction (i.e., heterojunction) among different components.

ZSH exhibits face-centered-cubic closed packing. Each microcube of ZSH-1 has six {100} facets, each micro-octahedrons of ZSH-3 have eight {111} facets, while each 14-facets polyhedron (including both truncated cube and truncated octahedron) of ZSH-2 has six {100} facets and eight {111} facets [17]. The crystal structure of  $\text{ZnSn}(\text{OH})_6$  with exposed {111} facet and {100} facet is shown in Fig. 10a. The valence and conduction band edges for the {100} facet present a higher barrier than that of the {111} facet [44]. The energy barrier, related to the surface atom density, the electronic structure and the bonding energy, can affect the photo-excited electrons from migrating across the interface. Therefore, it can be inferred that the photo-excited plasmonic electrons obtained from Bi nanoparticles via the transfer of oxygen vacancies (OV) in BiOCl (Fig. 10b) can be more easily injected into the {111} facets of ZSH due to the low energy barrier. The photo-generated electrons and holes can easily reach the particle surfaces for facile radical formation, resulting in much higher photocatalytic activity. The charge migration during the photocatalysis process was verified by photocurrent response. A comparison of the photocurrent density versus time curves for the as-prepared photocatalysts under intermittent visible light irradiation ( $\lambda > 420 \text{ nm}$ ) is displayed in Fig. 10c. For pure ZSH-3, photocurrent is negligible. For the composites, all of three photoelectrodes reveal stable and reversible photocurrent response. The immediate current signals right after the onset of light on demonstrate the high sensitivity to light. The order of photocurrent intensity is as follows: ZSH-3-Bi > ZSH-2-Bi > ZSH-1-Bi. After the introduction of Bi and BiOCl, the exposed {111} facets of ZSH was more favorable than that of {100} facets in charge separation, and thus resulted in much higher photocatalytic activity. Future work in this respect is still necessary to understand the mechanism.

The effect of UV-irradiation duration during the synthesis of composites has been presented in Fig. 9c. With the increasing exposure time from 1 h to 3 h, the materials color becomes more darker, revealing that the greater amounts of metallic Bi deposited on supporter. The XPS result shows that the content of Bi increases from 3.51% to 5.42% with the increasing exposure time. The longer the UV exposure duration is, the lower is the degradation efficiency. This phenomenon is presumably because the excess Bi nanoparticles on the composite could act as the recombination center for the photo-generated charges, thus leading to a decreased photocatalytic activity [58].

### 3.3. Photocatalytic mechanism

To evaluate the photo-degradation mechanism, the main oxidative species in the photocatalytic process was firstly detected through radical and hole trapping experiments using sodium oxalate (i.e.,  $\text{h}^+$  scavenger), *p*-benzoquinone (i.e.,  $\bullet\text{O}_2^-$  scavenger) or  $\text{N}_2$  flow (i.e., excluding  $\text{O}_2$ ). The  $\text{N}_2$  is purged through the RhB solution to remove the dissolved  $\text{O}_2$  in order to measure the formation of  $\bullet\text{O}_2^-$  radicals. As shown in Fig. 11a, the photocatalytic degradation of RhB is apparently restrained after the injection of sodium oxalate, *p*-benzoquinone or  $\text{N}_2$ . The rate constant ( $k$ ) reduces from  $0.01952 \text{ min}^{-1}$  in the photocatalytic system without any scavengers to  $0.00426 \text{ min}^{-1}$ ,  $0.00614 \text{ min}^{-1}$  and  $0.00019 \text{ min}^{-1}$  in the presence of  $\text{N}_2$ , *p*-benzoquinone and sodium oxalate, respectively. A greater reduction of  $k$  is related to the greater importance of the role of the corresponding oxidative species in the reaction. This indicates that the RhB degradation depends on both

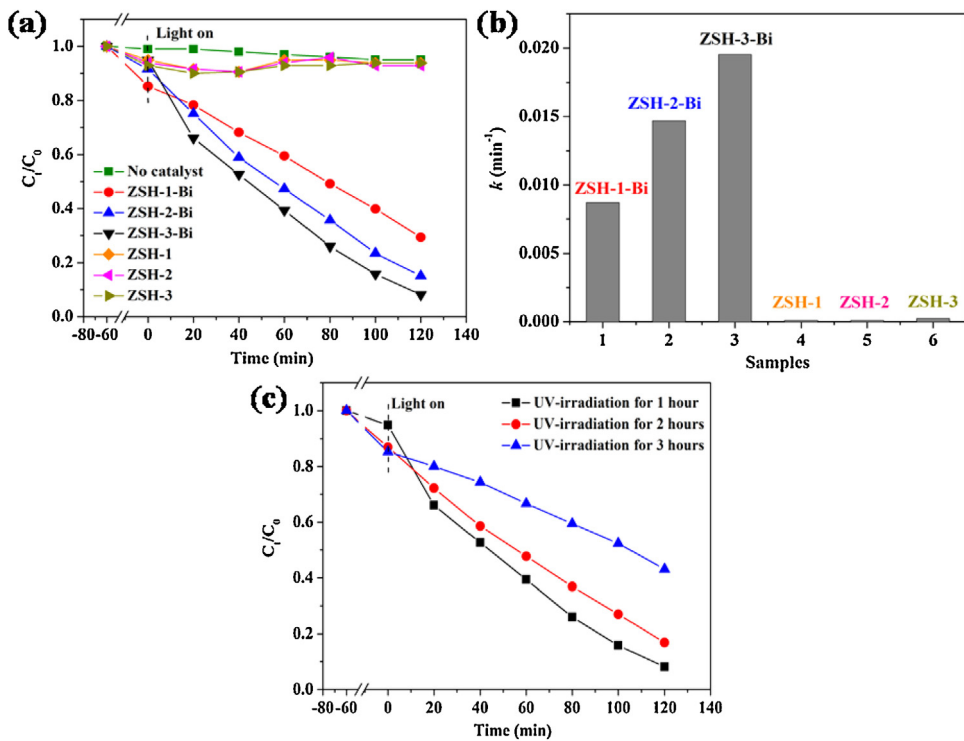


**Fig. 9.** (a) Photocatalytic RhB degradation performance with respect to time; (b) degradation rate constants based on pseudo-first order kinetics; and (c) the effect of UV irradiation duration during the synthesis of ZSH-3-Bi on photocatalytic performance.

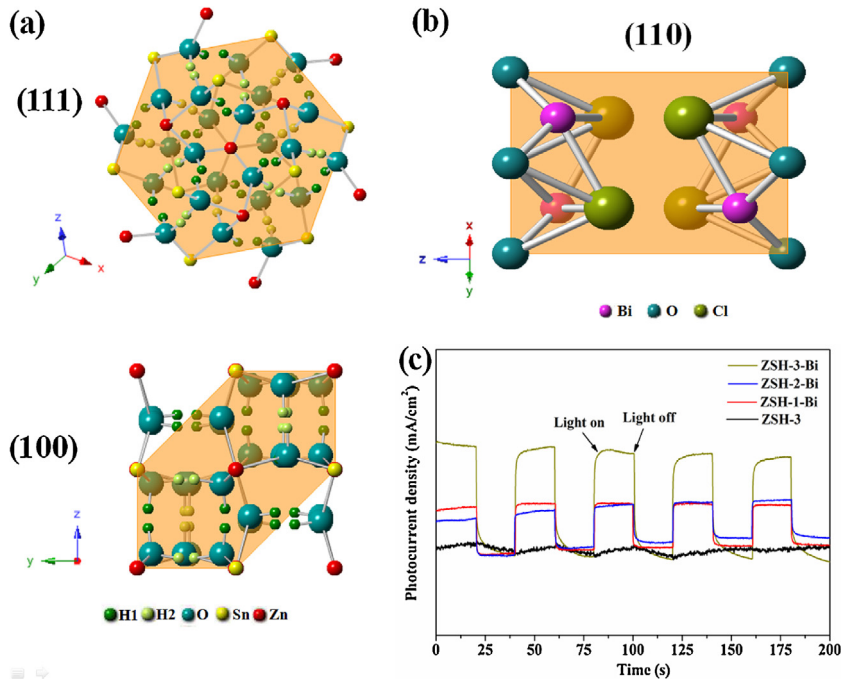


**Fig. 10.** (a) Crystal structure of  $\text{ZnSn}(\text{OH})_6$  with exposed {111} facet and {100} facet. (b) Crystal structure of  $\text{BiOCl}$  with exposed {110} facet. (c) Photocurrent (PC) response analysis of pure ZSH-3, ZSH-1-Bi, ZSH-2-Bi and ZSH-3-Bi under intermittent visible light irradiation ( $\lambda > 420 \text{ nm}$ ).

holes ( $\text{h}^+$ ) and  $\cdot\text{O}_2^-$  greatly. More interestingly, Fig. 11a further shows that the efficiency of the degradation is enhanced in the presence of isopropyl alcohol and tert-butanol, with the rate constant ( $k$ ) improving from  $0.01952 \text{ min}^{-1}$  without any scavengers to  $0.04977 \text{ min}^{-1}$  or  $0.03787 \text{ min}^{-1}$ , respectively. Isopropyl alcohol and tert-butanol are generally the sacrificial agents of  $\cdot\text{OH}$  radical; the enhancement of photocatalytic activity may mean that the for-

mation of  $\cdot\text{OH}$  radicals at the surface of the ZSH-3-Bi film is mainly dependent on electron-transfer mediation, which is because the photo-generated holes are scavenged by isopropyl alcohol and tert-butanol due to selective oxidation [59]. The photo-generated electrons can easily diffuse to the surface of the ZSH-3-Bi to form  $\cdot\text{OH}$  radical, leading to the degradation of RhB.

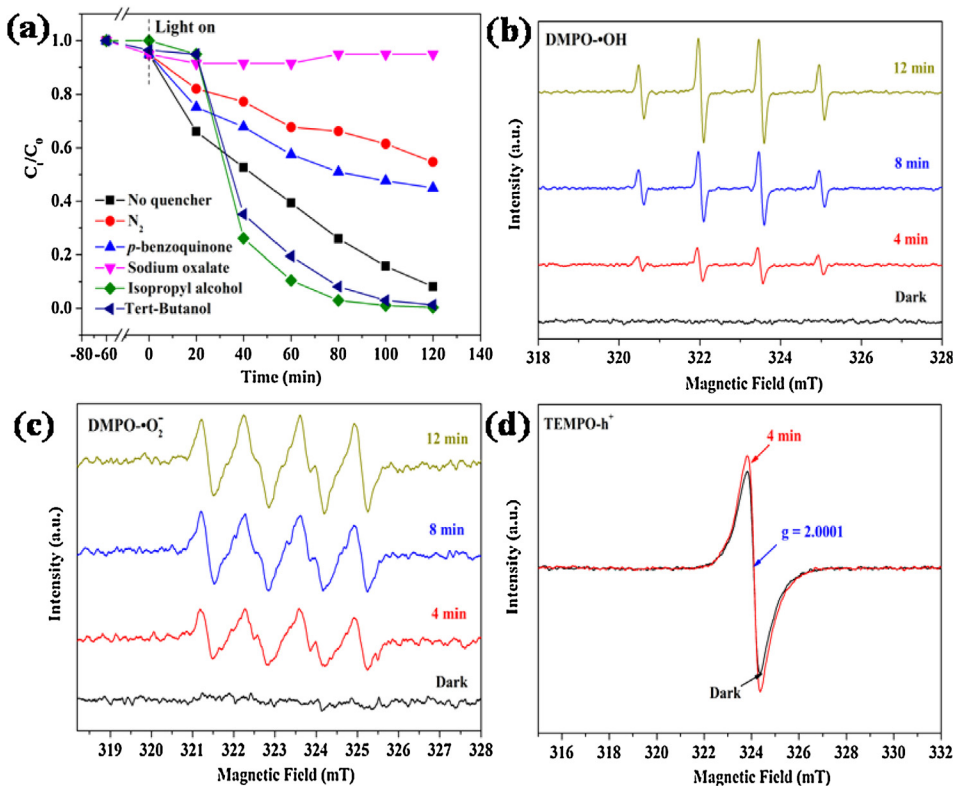


**Fig. 11.** (a) Effects of different reactive species scavengers on the photo-degradation of RhB by ZSH-3-Bi under visible-light irradiation. ESR spectra of radical adducts trapped by DMPO- $\cdot\text{O}_2^-$  and  $\cdot\text{OH}$  and TEMPO- $\text{h}^+$  in dispersion in the dark and under visible light irradiation: (b) in aqueous dispersion for DMPO- $\cdot\text{OH}$ ; (c) in methanol dispersion for DMPO- $\cdot\text{O}_2^-$  and (d) in aqueous dispersion for TEMPO- $\text{h}^+$ .

In order to confirm the  $\cdot\text{OH}$  radical generation in the photocatalytic system under visible light irradiation, the ESR spin-trap experiments were performed on the ZSH-3-Bi composite. All the experiments were operated in darkness and visible light irradiation durations of 4 min, 8 min and 12 min. As shown in Fig. 11b, the intensity of the DMPO- $\cdot\text{OH}$  adducts is negligible in the dark condition but become greater with longer durations of visible light irradiation, demonstrating that  $\cdot\text{OH}$  plays an important role in the photocatalytic process. Four characteristic peaks (Fig. 11c) of DMPO- $\cdot\text{O}_2^-$  are also observed in methanol dispersion under visible light irradiation, indicating that  $\cdot\text{O}_2^-$  is also produced. Furthermore, the holes ( $\text{h}^+$ ) of the photocatalysts are also tested. The intensities of the peaks of the spin-trapped TEMPO- $\text{h}^+$  (Fig. 11d) increase slightly when exposed to visible light irradiation relative to that in the dark. The characteristic signal at a  $g$ -value (i.e., the spectral splitting factor) of 2.0001 is also detected, providing evidence of oxygen vacancies (OV) located at the surface [32,60].

The results here validate that the holes ( $\text{h}^+$ ) or oxygen vacancies on the surface of ZSH-3-Bi participate in the photocatalytic process, which is also consistent with the above hole trapping experiments. Combining the trapping experiment and ESR analysis, it can be inferred that the main active species participating in the photocatalytic system are  $\cdot\text{OH}$ ,  $\cdot\text{O}_2^-$  and  $\text{h}^+$ . Three-dimensional (3D) EEMs (excitation-emission matrix fluorescence spectra) were employed to characterize the residual RhB solution after the photocatalytic process. Four samples were collected after different visible light irradiation durations of 0 min, 40 min, 80 min and 120 min. According to the 3D EEMs contour plots in Fig. 12, before irradiation, the RhB solution mainly contain four kinds of fluorescence peaks. As the visible light irradiation duration lengthen, three of the peaks disappear gradually and only one peak at  $E_x/E_m = 450-550/500-600$  nm existed at 120 min. The density (height) of this peak increased sharply from 1976 to 4689 within the

120 min, which may be attributed to photo-transformation intermediates, such as hydroxy derivatives. The change of fluorescence peaks is presumably because decolorization is the predominant reaction. Further, total organic carbon (TOC) test demonstrated that a relatively low mineralization rate of 16.7% TOC removal has been obtained after 120 min of irradiation, indicating that the RhB is partly transformed into  $\text{CO}_2$  and water. Therefore, in the photocatalytic reaction, RhB is mainly decoloured and part of the RhB molecule is mineralized into  $\text{CO}_2$  or  $\text{H}_2\text{O}$  during the visible light irradiation.

To give more definite insights into the photocatalysis mechanism of ZSH-3-Bi, the band edge positions of the conduction band (CB) and valence band (VB) of ZSH-3 in the ZSH-3-Bi composite at the point of zero charge can be theoretically predicted with the following formulas [18,61]:

$$E_{\text{CB}} = X - E_e - 0.5 E_g \quad (1)$$

$$E_{\text{VB}} = E_{\text{CB}} + E_g \quad (2)$$

where  $E_{\text{CB}}$ ,  $E_{\text{VB}}$ ,  $X$ ,  $E_e$  and  $E_g$  are the conduction band potentials, valence band potentials, absolute electronegativity, energy of free electrons and band gap energy, respectively. It is calculated that the  $E_{\text{CB}}$  and  $E_{\text{VB}}$  values of ZSH-3 are 0.31 eV and 3.45 eV, respectively. As for  $\text{BiOCl}$ ,  $E_{\text{CB}}$  and  $E_{\text{VB}}$  values are reported as -1.1 eV and 2.3 eV, respectively [32]. Because the Fermi level of the metal Bi is -0.17 eV, the band structure and the photo-excited electron-hole separation process can be proposed, as shown in Fig. 13. In the photocatalytic reaction process, the SPR effect of metallic Bi does not only propel the ZSH-3-Bi to absorb more visible light, but also photo-excite Bi nanoparticles, thereby enhancing the surface electron excitation and interfacial electron transfer [35]. The Fermi level of metal Bi is matched with the position of oxygen vacancies (OV) in  $\text{BiOCl}$ , which is conducive to the electron transfer from Bi nanoparticles

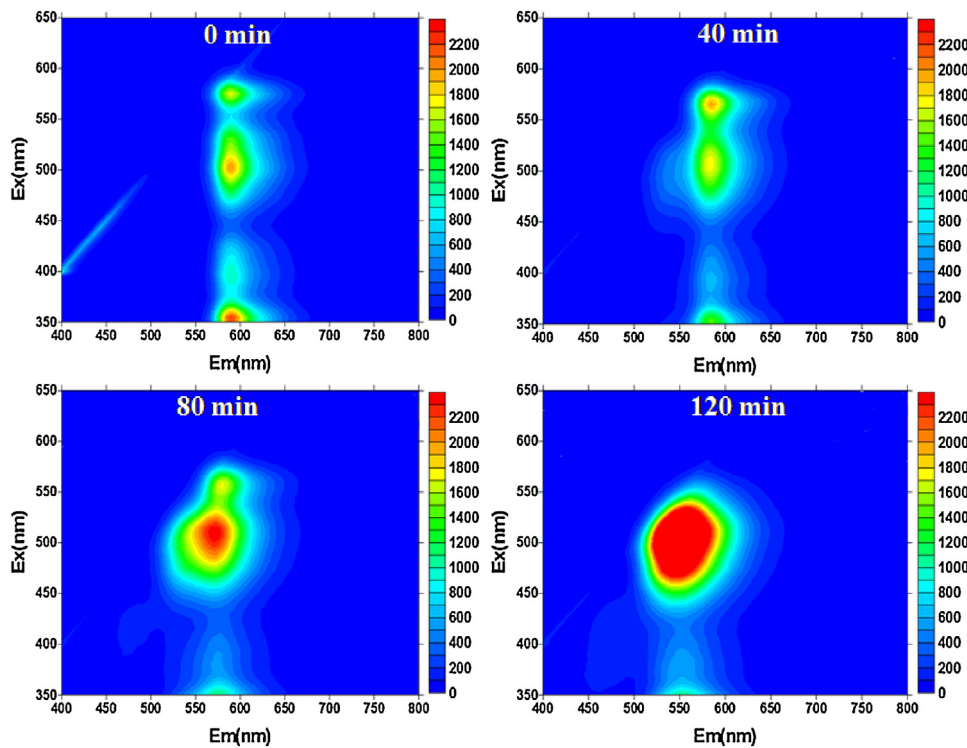


**Fig. 12.** Three-dimensional excitation-emission matrix fluorescence spectra (3D EEMs) of the residual RhB solution after visible light irradiation durations of 0 min, 40 min, 80 min and 120 min.

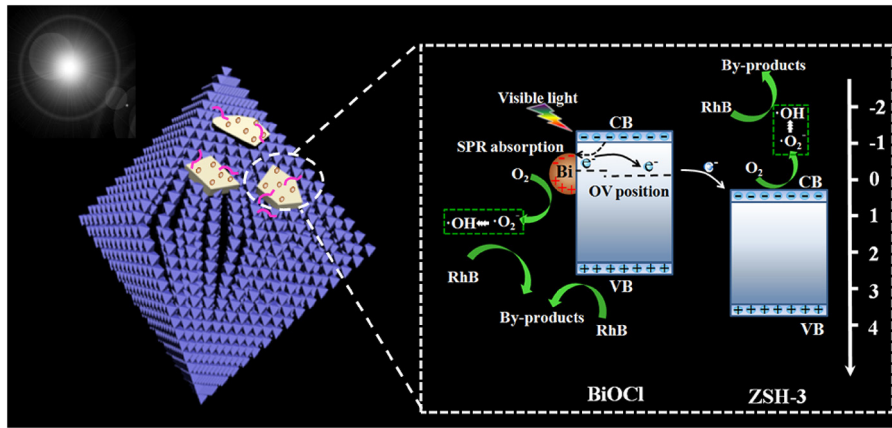


**Fig. 13.** The proposed band structure and photocatalytic mechanism of ZSH-3-Bi.

to BiOCl sheets [32]. The electron is stabilized by creating more oxygen vacancy states, as demonstrated by the TEMPO- $h^+$  signal (Fig. 11d). Then the electrons are rapidly transferred to the conduction band (CB) of ZSH, the accumulated electrons are trapped by dissolved oxygen to form radical dot  $\cdot O_2^-$ , and subsequently produce  $\cdot OH$  [46]. The photo-induced  $\cdot OH$  and  $\cdot O_2^-$  then plays a role in the RhB degradation. Simultaneously, the electrons-donator Bi nanoparticles shift to more positive potentials to produce positive charges, and accept electrons from the VB of BiOCl to return to its initial state, which is analogous to the Ag co-catalyst in photocatalysis [37]. Herein, metallic Bi can also serve as an electron trap to facilitate the separation of the photo-excited carriers and promote the interfacial electron transfer process. The electron acceptors, like adsorbed  $O_2$ , can easily trap the electrons to produce  $\cdot O_2^-$  radical. Moreover, the holes in BiOCl can also directly react with the RhB molecule when they are captured by the organic compound on the BiOCl surface [53]. As a result, the photocatalytic performance is

significantly enhanced and the RhB is degraded through the  $\cdot O_2^-$ ,  $\cdot OH$ , or direct  $h^+$  oxidation pathways. In this proposed mechanism, BiOCl functions as an electronic modulator for the electron-transfer process with the aid of valence band (VB) and oxygen defect structures.

#### 4. Conclusion

A novel plasmonic Bi nanoparticles and BiOCl sheets co-decorated  $ZnSn(OH)_6$  (ZSH) with various morphologies (hence exposure facets) was successfully synthesized via one-pot precipitation, hydrolysis and UV-photoreduction process. The photocatalyst exhibited an improved photocatalytic performance for the degradation of Rhodamine B under visible-light irradiation. The great RhB degradation rate was by ZSH-3-Bi, followed by ZSH-2-Bi, ZSH-1-Bi and pure ZSH. The photo-degradation rate of ZSH-3-Bi was about 81 times higher than that of pure ZSH-3. The high-

est photocatalytic performance was mainly ascribed to the surface plasmon resonance effect for visible light absorption, the exposed {111} facets relative to other facets of ZSH, and the improved charge carrier separation efficiency due to the strong interfacial interaction of the different components. The reactive species ( $\cdot\text{OH}$ ,  $\cdot\text{O}_2^-$  and  $\text{h}^+$ ) generated in the photocatalytic process led to the de-coloration and part mineralization of the RhB molecules. This work provides new insights into the one-pot in situ fabrication of non-noble metals Bi/semiconductor composites with facet-oriented polyhedron for full utilization of solar energy and wastewater treatment.

## Acknowledgments

The authors gratefully acknowledge the financial support provided by the Foundation for Innovative Research Groups of the National Natural Science Foundation of China (No. 51521006), the Key Project of National Nature Science Foundation of China (No. 71431006), and Key Research and Development Project of Hunan Province, China (No. 2016SK2015). We also acknowledge funding from the Singapore Ministry of Education Academic Research Funds Tier 2 (MOE2014-T2-2-074; ARC16/15) and Tier 1 (2015-T1-001-023; RG7/15).

## References

- [1] D.M. Schultz, T.P. Yoon, *Science* 343 (2014) 1239176.
- [2] M.H. Sun, S.Z. Huang, L.H. Chen, Y. Li, X.Y. Yang, Z.Y. Yuan, B.L. Su, *Chem. Soc. Rev.* 45 (2016) 3479–3563.
- [3] H. Wang, X. Yuan, Y. Wu, H. Huang, X. Peng, G. Zeng, H. Zhong, J. Liang, M. Ren, *Adv. Colloid Interface Sci.* 195–196 (2013) 19–40.
- [4] H. Wang, X. Yuan, G. Zeng, Y. Wu, Y. Liu, Q. Jiang, S. Gu, *Adv. Colloid Interface Sci.* 221 (2015) 41–59.
- [5] M. Saliba, T. Matsui, J.-Y. Seo, K. Domanski, J.-P. Correa-Baena, M.K. Nazeeruddin, S.M. Zakeeruddin, W. Tress, A. Abate, A. Hagfeldt, M. Gratzel, *Energy Environ. Sci.* 9 (2016) 1989–1997.
- [6] W. Wang, M.O. Tade, Z. Shao, *Chem. Soc. Rev.* 44 (2015) 5371–5408.
- [7] D.L. Jiang, T.Y. Wang, Q. Xu, D. Li, S.C. Meng, M. Chen, *Appl. Catal. B: Environ.* 201 (2017) 617–628.
- [8] E. Grabowska, *Appl. Catal. B: Environ.* 186 (2016) 97–126.
- [9] H. Wang, X. Yuan, *Environ. Sci. Pollut. Res. Int.* 21 (2014) 1248–1250.
- [10] W.H. Feng, Z.X. Pei, Z.B. Fang, M.L. Huang, M.L. Lu, S.X. Weng, Z.Y. Zheng, J. Hu, P. Liu, *J. Mater. Chem. A* 2 (2014) 7802–7811.
- [11] C.Y. Chen, X.Z. Zheng, J. Yang, M.D. Wei, *Phys. Chem. Chem. Phys.* 16 (2014) 20073–20078.
- [12] X.L. Fu, D.W. Huang, Y. Qin, L.F. Li, X.L. Jiang, S.F. Chen, *Appl. Catal. B: Environ.* 148 (2014) 532–542.
- [13] H.H. Zhang, P. Song, D. Han, H.H. Yan, Z.X. Yang, Q. Wang, *Sens. Actuator B: Chem.* 209 (2015) 384–390.
- [14] X. Fu, X. Wang, Z. Ding, D.Y.C. Leung, Z. Zhang, J. Long, W. Zhang, Z. Li, X. Fu, *Appl. Catal. B: Environ.* 91 (2009) 67–72.
- [15] Y. Chen, D. Li, M. He, Y. Hu, H. Ruan, Y. Lin, J. Hu, Y. Zheng, Y. Shao, *Appl. Catal. B: Environ.* 113–114 (2012) 134–140.
- [16] H. Lu, J. Lei, X. Li, G. Shao, T. Hou, B. Fan, D. Chen, L. Zhang, H. Wang, H. Xu, R. Zhang, *Cryst. Res. Technol.* 51 (2016) 11–15.
- [17] H. Yu, R. Lai, H. Zhuang, Z. Zhang, X. Wang, *CrystEngComm* 14 (2012) 8530–8535.
- [18] F. Chen, Q. Yang, X. Li, D. Wang, Y. Zhong, J. Zhao, Y. Deng, C. Niu, G. Zeng, *Catal. Commun.* 84 (2016) 137–141.
- [19] F. Chen, Q. Yang, C.G. Niu, X.M. Li, C. Zhang, J.W. Zhao, Q.X. Xu, Y. Zhong, Y.C. Deng, G.M. Zeng, *Catal. Commun.* 73 (2016) 1–6.
- [20] H. Li, Y. Cui, W. Hong, B. Xu, *Chem. Eng. J.* 228 (2013) 1110–1120.
- [21] J.M. Wu, Y.N. Chen, *Dalton Trans.* 44 (2015) 16294–16303.
- [22] L. Tang, G.-M. Zeng, G.-L. Shen, Y.-P. Li, Y. Zhang, D.-L. Huang, *Environ. Sci. Technol.* 42 (2008) 1207–1212.
- [23] X. Yuan, H. Wang, Y. Wu, G. Zeng, X. Chen, L. Leng, Z. Wu, H. Li, *Adv. Organomet. Chem.* 30 (2016) 289–296.
- [24] J. Toudert, R. Serna, M. Jiménez de Castro, *J. Phys. Chem. C* 116 (2012) 20530–20539.
- [25] J. Zhao, Q. Han, J. Zhu, X. Wu, X. Wang, *Nanoscale* 6 (2014) 10062–10070.
- [26] F. Gao, Y. Zhao, Y. Li, G. Wu, Y. Lu, Y. Song, Z. Huang, N. Li, J. Zhao, *J. Colloid Interface Sci.* 448 (2015) 564–572.
- [27] F. Dong, T. Xiong, Y. Sun, Z. Zhao, Y. Zhou, X. Feng, Z. Wu, *Chem. Commun.* 50 (2014) 10386–10389.
- [28] K. Ji, H. Dai, J. Deng, H. Zang, H. Arandiyan, S. Xie, H. Yang, *Appl. Catal. B: Environ.* 168–169 (2015) 274–282.
- [29] K. Ji, J. Deng, H. Zang, J. Han, H. Arandiyan, H. Dai, *Appl. Catal. B: Environ.* 165 (2015) 285–295.
- [30] H. Jiang, H. Dai, X. Meng, K. Ji, L. Zhang, J. Deng, *Appl. Catal. B: Environ.* 105 (2011) 326–334.
- [31] F. Dong, Z. Zhao, Y. Sun, Y. Zhang, S. Yan, Z. Wu, *Environ. Sci. Technol.* 49 (2015) 12432–12440.
- [32] Y. Yu, C. Cao, H. Liu, P. Li, F. Wei, Y. Jiang, W. Song, *J. Mater. Chem. A* 2 (2014) 1677–1681.
- [33] Y. Gao, Y. Huang, Y. Li, Q. Zhang, J.-j. Cao, W. Ho, S.C. Lee, *ACS Sustain. Chem. Eng.* 4 (2016) 6912–6920.
- [34] Y. Sun, Z. Zhao, F. Dong, W. Zhang, *Phys. Chem. Chem. Phys.* 17 (2015) 10383–10390.
- [35] F. Dong, Q. Li, Y. Sun, W.-K. Ho, *ACS Catal.* 4 (2014) 4341–4350.
- [36] T. Xiong, X.a. Dong, H. Huang, W. Cen, Y. Zhang, F. Dong, *ACS Sustain. Chem. Eng.* 4 (2016) 2969–2979.
- [37] S. Xiao, Y. Li, J. Hu, H. Li, X. Zhang, L. Liu, J. Lian, *CrystEngComm* 17 (2015) 3809–3819.
- [38] X. Liu, H. Cao, J. Yin, *Nano Res.* 4 (2011) 470–482.
- [39] H. Zeynali, S. Behnam Mousavi, S.M. Hosseinpour-Mashkani, *Mater. Lett.* 144 (2015) 65–68.
- [40] Z. Zhao, W. Zhang, Y. Sun, J. Yu, Y. Zhang, H. Wang, F. Dong, Z. Wu, *J. Phys. Chem. C* 120 (2016) 11889–11898.
- [41] Y. Huang, S. Kang, Y. Yang, H. Qin, Z. Ni, S. Yang, X. Li, *Appl. Catal. B: Environ.* 196 (2016) 89–99.
- [42] X. Zhu, Z. Liu, J. Fang, S. Wu, W. Xu, *J. Mater. Res.* 28 (2013) 1334–1342.
- [43] L. Liu, W. Yang, W. Sun, Q. Li, J.K. Shang, *ACS Appl. Mater. Interfaces* 7 (2015) 1465–1476.
- [44] G.Z. Yuan, C.F. Hsia, Z.W. Lin, C. Chiang, Y.W. Chiang, M.H. Huang, *Chem. Eur. J.* 22 (2016) 12548–12556.
- [45] H. Wang, X. Yuan, Z. Wu, L. Wang, X. Peng, L. Leng, G. Zeng, *Sep. Sci. Technol.* 49 (2014) 2689–2699.
- [46] H. Wang, X. Yuan, Y. Wu, G. Zeng, H. Dong, X. Chen, L. Leng, Z. Wu, L. Peng, *Appl. Catal. B: Environ.* 186 (2016) 19–29.
- [47] D.-L. Huang, G.-M. Zeng, C.-L. Feng, S. Hu, X.-Y. Jiang, L. Tang, F.-F. Su, Y. Zhang, W. Zeng, H.-L. Liu, *Environ. Sci. Technol.* 42 (2008) 4946–4951.
- [48] L. Kong, Z. Jiang, H.H.C. Lai, T. Xiao, P.P. Edwards, *Prog. Nat. Sci. Mater. Int.* 23 (2013) 286–293.
- [49] H. Meng, T. Wang, X. Yu, Y. Zhu, Y. Zhang, *RSC Adv.* 5 (2015) 107088–107097.
- [50] Z. Shi, Y. Wang, C. Fan, Y. Wang, G. Ding, *Trans. Nonferrous Met. Soc. China* 21 (2011) 2254–2258.
- [51] H. Wang, X. Yuan, Y. Wu, X. Chen, L. Leng, G. Zeng, *RSC Adv.* 5 (2015) 32531–32535.
- [52] Z.Q. Li, X.T. Chen, Z.L. Xue, *CrystEngComm* 15 (2013) 498–508.
- [53] J. Hu, G. Xu, J. Wang, J. Lv, X. Zhang, Z. Zheng, T. Xie, Y. Wu, *New J. Chem.* 38 (2014) 4913–4921.
- [54] X. Guo, M. Cai, R. Li, X. Han, *CrystEngComm* 18 (2016) 6608–6613.
- [55] Z. Haider, J.Y. Zheng, Y.S. Kang, *Phys. Chem. Chem. Phys.* 18 (2016) 19595–19604.
- [56] Z. Wang, C. Jiang, R. Huang, H. Peng, X. Tang, *J. Phys. Chem. C* 118 (2014) 1155–1160.
- [57] H. Wang, X. Yuan, Y. Wu, G. Zeng, X. Chen, L. Leng, H. Li, *Appl. Catal. B: Environ.* 174–175 (2015) 445–454.
- [58] S. Weng, B. Chen, L. Xie, Z. Zheng, P. Liu, *J. Mater. Chem. A* 1 (2013) 3068–3075.
- [59] J. Zhuang, W. Dai, Q. Tian, Z. Li, L. Xie, J. Wang, P. Liu, X. Shi, D. Wang, *Langmuir* 26 (2010) 9686–9694.
- [60] Q. Zhao, X. Wang, T. Cai, *Appl. Surf. Sci.* 225 (2004) 7–13.
- [61] Y. Liu, X. Yuan, H. Wang, X. Chen, S. Gu, Q. Jiang, Z. Wu, L. Jiang, Y. Wu, G. Zeng, *Catal. Commun.* 70 (2015) 17–20.